Quantitative analysis of the debonding structure of soft adhesives

François Tanguy, Matteo Nicoli, Anke Lindner, Costantino Creton

Regular Article

Quantitative analysis of the debonding structure of soft adhesives

François Tanguy[1], Matteo Nicoli[1,2,a], Anke Lindner[3,b], and Costantino Creton[1]

[1] Laboratoire de Physico-Chimie des Polymeres et Milieux Disperses, UMR7615 ESPCI-CNRS-UPMC, 10 rue Vauquelin, 75005 Paris, France
[2] Laboratoire de Physique de la Matière Condensée, École Polytechnique-CNRS, 91128 Palaiseau, France
[3] Laboratoire de Physique et Mécanique des Milieux Hétérogenes, UMR7636 CNRS/ESPCI Paristech, Université Pierre et Marie Curie, Université Paris Diderot, 10 rue Vauquelin, 75005 Paris, France

Abstract. We experimentally investigate the growth dynamics of cavities nucleating during the first stages of debonding of three different model adhesives. The material properties of these adhesives range from a more liquid-like material to a soft viscoelastic solid and are carefully characterized by small strain oscillatory shear rheology as well as large strain uniaxial extension. The debonding experiments are performed on a probe tack set-up. Using high contrast images of the debonding process and precise image analysis tools, we quantify the total projected area of the cavities, the average cavity shape and growth rate and link these observations to the material properties. These measurements are then used to access corrected effective stress and strain curves that can be directly compared to the results from the uniaxial extension.

1 Introduction

When soft adhesives are detached from rigid surfaces, the incompressibility of the material combined to its extreme deformability leads to complex deformation patterns involving the formation of air fingers and cavities [1–5]. The details of these patterns depend markedly on the material properties and often evolve towards a fibrillar structure of highly stretched polymers which eventually fail by fracture or detach from the surface [6]. The criteria for the onset of the initial elastic or viscous instabilities have been known for some time [7,8] and several experimental studies have focused on fingering instabilities [8–10], on the cavitation criteria [11–15], cavity nucleation rate [16,17] or growth rate [18]. However the transition from growth of individual cavities to the collective growth of a population of cavities under the applied stress, leading to elongated walls between cavities, also called "fibrils" and to eventual detachment, has received much less attention experimentally [16,17]. Some theoretical papers have been published on collective growth [19,20].

Up to date, it remains difficult to relate the observed patterns to the rheological properties of the soft adhesives, mainly due to the lack of precise experimental characterization of the 3D structures and of the material deformation during the debonding process. Because the processes are dynamic, powerful 3D scanning techniques, such as confocal microcopy, are too slow and one has to rely on classical 2D imaging limited by its depth of field. Proper identification of the cavity borders in an automatic and reliable way is not a trivial task and requires good-quality well-contrasted images and adapted imaging software tools. Yet, this information, albeit statistical in nature, is essential if one wishes to gain more insights on the debonding process and to be able to compare experiments with results from numerical simulations. It is also a necessary ingredient to understand which rheological properties of the material determine the debonding patterns and, eventually, the adhesion performance, the important parameter for practical applications.

In this paper we have performed careful experiments yielding high contrast images of the cavities nucleated in the early stages of debonding during a probe tack test. We have developed precise image analysis tools to characterize quantitatively and in a statistically significant way the size, shape and overall projected surface of the cavities. Using model materials with well known rheological properties, spanning from viscoelastic liquids to viscoelastic solids, we will present detailed measurements of the growth dynamics of cavities, including the total projected area, the average cavity shape and their growth rate. These measurements give access to a corrected true or effective stress and strain which can then be quantitatively compared with material properties in shear and uniaxial extension.

[a] *Present address*: Center for Interdisciplinary Research on Complex Systems, Department of Physics, Northeastern University, Boston, MA 02115, USA.
[b] e-mail: anke.lindner@espci.fr

Table 1. Properties of the model acrylic polymers. The parameter d_0 is the diameter of the particles, see the main text for additional details.

Polymer	CTA	Mw	PDI	d_0	Gel content
	(%)	(kg/mol)	(-)	(nm)	(%)
Bg1110	-	1115	3.39	368	30
A1570	-	1572	2.57	400	-
A650	0.1	651	2.18	400	-

2 Materials and methods

2.1 Sample preparation

Model acrylate random copolymers containing 98.1% of butyl acrylate and 1.9% of acrylic acid and with varying molecular weights were synthesized by emulsion polymerization by The Dow Chemical Company. Two series (A and B) were produced by changing the conditions of synthesis in order to obtain different architectures and, thus, a wide range of viscoelastic properties. Chain Transfer Agent (CTA) was used to control the weight average molecular weight, Mw, of the samples for a given series. For each sample we characterized its Mw and gel content. The average particle size was found to be around 380 nm, see table 1. It was determined by The Dow Chemical Company that all polymers have a low proportion of short branches.

Latex solutions have been dried using two different techniques for mechanical and adhesion tests described below. Rheology and tensile tests required thick films ($\sim 600\,\mu m$), so that latexes were cast in silicone molds and dried during a week at room temperature followed by 5 min at 110 °C in an oven. For adhesion tests, thin films ($\sim 140\,\mu m$) coated on glass slides were made. In this case, latexes were cast on glass slides and dried for 24 hours at room temperature followed by 2 min at 110 °C in an oven. In both cases transparent cohesive films were obtained showing a good coalescence of the particles of the latex.

2.2 Rheology and probe tack test set-up

The characterization of the viscoelastic properties of the polymers was done on an ARES rheometer (TA) with a standard plate geometry at the Université Catholique de Louvain (UCL). The frequency range was between 10^{-2} and $10^2\,\mathrm{rad\,s^{-1}}$, while the temperature ranged from -30 to 90 °C. We also performed tensile tests to obtain the mechanical properties of the sample in uniaxial extension. Experiments were carried out in a standard tensile Instron equipment (5565) equipped with a videoextensometer (SVE). We imposed two different cross-head velocities v, 1.05 and 0.105 $\mathrm{mm\,s^{-1}}$, for samples with an initial length l_0 of 15 mm and an initial cross section $S_0 = 2.5\,\mathrm{mm^2}$, resulting in a nominal initial strain rate

v/l_0 of 0.07 and 0.007 Hz, respectively (all the symbols used in the main text are reported in table 2).

A home-built "probe tack" set up [21] was employed to observe the deformation structure of the soft adhesives and to measure force and displacement during debonding. The apparatus consists of a cylindrical flat-ended probe brought into contact with an adhesive layer at a given speed of $30\,\mu\mathrm{m\,s^{-1}}$ until a force of 20 N, corresponding to an applied pressure of 0.18 MPa, is reached. After a contact time of 10 s, the probe was pulled away at a constant rate V of 1 or $10\,\mu\mathrm{m\,s^{-1}}$. The nominal force F_T and displacement d were measured during the whole experiment. d corresponds to the displacement of the adhesive layer and is obtained via a displacement sensor, measuring the relative displacement between the probe and the sample holder. The output of the displacement sensor was corrected for the compliance of the glass slide holding the sample to obtain directly the displacement of the adhesive layer [22]. As the initial thickness of the sample h_0 is $140\,\mu m$, the nominal strain rate approximated by V/h_0 was 0.007 and 0.07 Hz, respectively. The probe was made of stainless steel, a material that offers a high surface energy and leads to good adhesion. Furthermore, in order to obtain a perfectly smooth and reflective surface, the probe was mechanically polished. In all the experiments we used a probe with a diameter of 6 mm.

A microscope was coupled to this experiment in order to observe the debonding structure from the top. A camera (resolution of 1292×964 pixels) numerically recorded the digitalized images. Two Zeiss lenses ($1.25\times$ and $5\times$) were used in order to get low or high magnification images, with a field of view of $7.34 \times 5.48\,\mathrm{mm}$ and $1.92 \times 1.44\,\mathrm{mm}$, respectively. Images and force-displacement data were synchronized with a trigger to start simultaneously the probe-tack experiment and the image acquisition process. This trigger also controlled the frequency of the acquisition of the images, setting a frame rate of 10 and 20 fps for a velocity of 1 and $10\,\mu\mathrm{m\,s^{-1}}$, respectively.

2.3 Image analysis

Quantitative information about the nucleation and the growth of cavities can be obtained by processing the digitalized top-view images acquired in probe-tack experiments. We developed a simple method to analyze these images using standard routines already available in many packages for image processing, such as the Image Processing Toolbox™ for Matlab® or the public domain software ImageJ. An example of the result of this procedure is shown in fig. 1.

The algorithm detects all cavities with a surface larger than a threshold $\epsilon_A = 50$ pixels. Several geometrical quantities, such as the center of mass, the area, the equivalent diameter and the eccentricity are measured for each cavity. The program also assigns an index to each cavity and by comparing the center of mass of cavities between two subsequent frames, nucleation and coalescence events can be tracked. For additional details see appendix A.

Table 2. List of symbols used in the manuscript.

Uniaxial Extension	l_0	Initial sample length	S_0	Initial cross section	
	σ_N	Nominal stress	σ_T	True stress	
Probe-tack	h_0	Initial sample thickness	h	Time dependent sample thickness	
	λ	Nominal elongation	$\langle\lambda\rangle$	Effective elongation	
	A_0	Probe area	A_b	Area covered by cavities	
	A_e	Load-bearing area ($A_e + A_b = A_0$)	A_d	Total excess area, see sect. 3.4	
	A_c	Area of the convex envelope occupied by cavities, see sect. 3.6	F_T	Normal component of the force applied to A_0	
	F_m	Force applied to elongate the viscoelastic material	F_P	Work done against the atmospheric pressure to expand the cavities	
	P_{atm}	Atmospheric pressure	P_b	Pressure inside the cavities	
	σ_N	Nominal stress	σ_e	Effective tensile stress applied to the viscoelastic material	
	V	Pulling velocity			

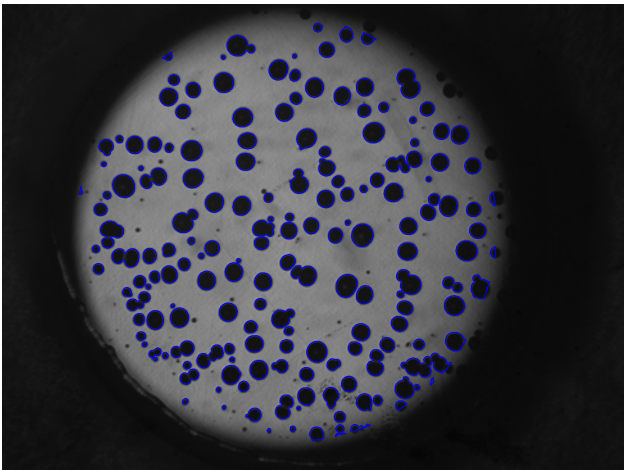**Fig. 1.** Processed top-view frame (field of view 7.34 mm × 5.48 mm) of the cavitation process. Blue contours represent the borders of the cavities our algorithm is able to detect. Only a few small cavities are missed because they are below the noise level. They will be tracked in the next frames when their area exceeds ϵ_A (see main text).

Fig. 2. Storage (G') and shear (G'') modulus as function of angular frequency (ω) for the three different materials [23].

3 Results and discussion

3.1 Mechanical properties

The three different materials studied differ only in architecture and molecular weight and the molecular interactions with a substrate should thus be the same for all three materials. Figure 2 shows master curves at 20 °C of G' and G'' as a function of angular frequency ω [23]. The curves were obtained by applying time-temperature superposition and it can be seen that the viscoelastic prop-
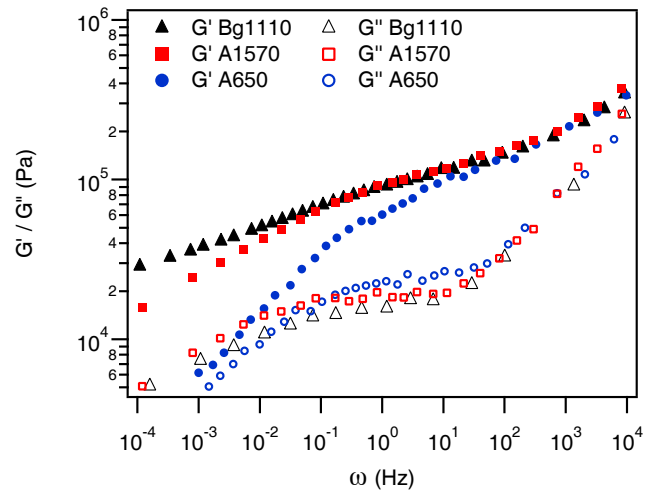
erties of the three materials are identical at frequencies f larger than 10 Hz. However, at low frequencies the rheology of A650 differs from the behavior found for A1570 and Bg1110. The elastic modulus of A650 decreases strongly at low frequency, leading to a material with a pronounced viscoelastic character. A1570 and Bg1110 on the other hand can be described as soft viscoelastic solids over the whole range of frequencies. No terminal flow was detected for any material within the range of frequencies investigated.

While linear viscoelastic properties characterize time-dependent relaxation processes, strain-dependent behavior is characterized using large strain properties measured at a given strain rate. In uniaxial extension at a
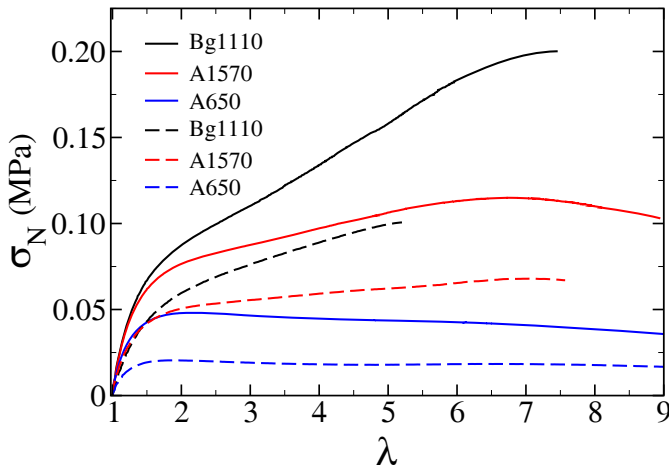
Fig. 3. Nominal stress *versus* elongation in tensile test for an elongation rate $\dot{\lambda}_z = 0.07\,\mathrm{s}^{-1}$ (solid lines) and $\dot{\lambda}_z = 0.007\,\mathrm{s}^{-1}$ (dashed lines).

fixed crosshead velocity, the materials show pronounced differences in the experimental curves of nominal stress $\sigma_N = F/S_0$ *versus* the elongation of the sample $\lambda = l(t)/l_0$ (see fig. 3). Macroscopic flow is observed for the most viscoelastic material, *i.e.* the A650 series, while a slight strain hardening behavior characterizes the Bg1110 adhesive. Although A1570 and Bg1110 have identical linear viscoelastic properties at frequencies above 0.01 Hz, the presence of a gel fraction in the Bg1110 series results in a different large-strain behavior and we observe a markedly higher stress at large strain.

3.2 Adhesion properties

Probe tack tests were carried out at two probe velocities for the three materials. For all experiments, the adhesive films have an initial thickness h_0 and are pulled by a cylindrical probe of area A_0. Experiments were repeated several times and the force F_T and the displacement $d = h(t) - h_0$ as a function of time were measured. The nominal stress is given by

$$\sigma_N = \frac{F_T}{A_0}\,, \tag{1}$$

while

$$\lambda = \frac{h(t)}{h_0} \tag{2}$$

represents the nominal elongation of the whole sample in the vertical direction.

The experiments are filmed at low and high magnification to capture the dynamics of cavity nucleation and growth. During the displacement of the probe the volume between the probe and the glass slide expands. As the adhesive is incompressible and does not slip at the interface, this increase in volume leads to a large increase in tensile stress inside the layer and to the nucleation of cavities at the interface between the probe and the adhesive [24] and to their subsequent growth. Note that, as the volume of

the cavities expands, the pressure inside the cavities tends towards zero.

The nominal stress-strain curves $\sigma_N = f(\lambda)$ are shown in fig. 4 and are discussed together with the different dynamics of cavity growth. At a debonding rate of $10\,\mu\mathrm{m\,s}^{-1}$ (fig. 4a), three different shapes of stress-strain curves are observed for the three materials used. Bg1110, the most elastic material, shows a sharp stress peak, followed by a fast decrease of σ_N. This shape is explained by the nucleation of cavities during the increase in σ_N. These cavities first expand in the bulk of the layer but eventually coalesce at the interface with the substrate. This rapid coalescence leads to the fast decrease in nominal stress observed and results in interfacial debonding. For A1570, cavities also mainly nucleate during the initial increase of the nominal stress. At higher deformation the nominal stress is found to stabilize at a nearly constant value, characteristic of the growth of cavities in the bulk and the subsequent formation of elongated walls or fibrils. At the end, the fibrils detach from the surface, leading to an adhesive debonding. The experiment with A650 shows a double plateau, characteristic of liquid-like materials. In this case the walls formed between growing cavities are too liquid-like to sustain the pressure difference between the low pressure cavities and the atmospheric pressure and pressure equilibration takes place before final fibril detachment [14]. In this case cohesive failure, *i.e.* residues on the probe, are observed.

At $1\,\mu\mathrm{m\,s}^{-1}$ (fig. 4b), the shape of the stress-strain curve of the Bg1110 and A650 are qualitatively identical to those observed at $10\,\mu\mathrm{m\,s}^{-1}$ (fig. 4a) except for a decrease of the overall stress during debonding. For A1570, a transition is observed towards a liquid-like behavior with two plateaus.

3.3 Evolution of the load-bearing area

Due to the presence of cavities, the force applied on the disk-shape sample is effectively only applied on a load-bearing cross section that becomes increasingly smaller as λ increases. By analyzing the projected area covered by the cavities and subtracting it from the total contact area, this load-bearing area can be obtained. This will allow us to calculate (in the following section) the average true or effective stress applied, instead of the nominal stress studied in previous investigations [3,11,16,25].

By means of the image analysis method described in the previous section we can measure for each frame the total area covered by the cavities A_b and then subtract it from the area of the probe A_0, corresponding to the total contact area. Note that for our experiments no debonding takes place from the edges of the probe and the total contact area A_0 does thus not evolve during the experiment. In this way we deduce the load-bearing cross section of our disk as a function of time, $A_e(t) = A_0 - A_b(t)$. This latter quantity is simply the effective area of the walls between cavities. As the observation direction is normal to the disk, the maximal diameter of each cavity is observed in the projected image, see the sketch in fig. 5, and we thus
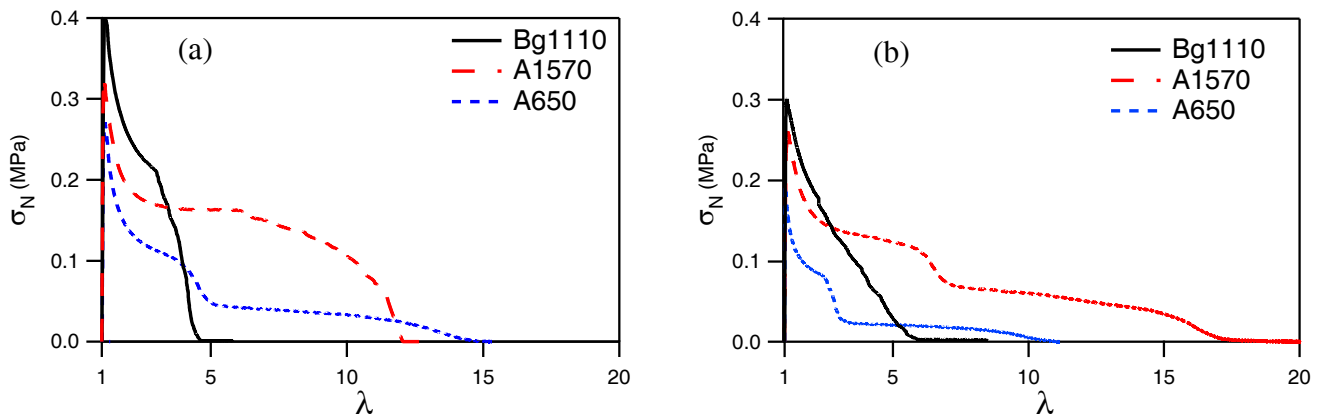
Fig. 4. Representative curves for nominal stress σ_N for the three materials as a function of the elongation λ at a pulling velocity of $10\,\mu\mathrm{m\,s}^{-1}$ (a) and $1\,\mu\mathrm{m\,s}^{-1}$ (b).
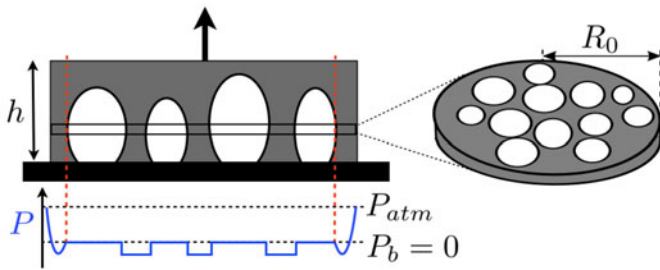

Fig. 5. Left: representation of the sample under deformation. The load-bearing area determined by the top-view analysis is represented by the slice shown on the right. The effective normal stress (sect. 3.6) and the effective elongation (sect. 3.7) are calculated for this slice and correspond to averages over the area of the slice. Bottom: sketch of a typical pressure distribution in the stretched adhesive layer containing cavities.

obtain the minimal projected area of the walls between the cavities. Note that the illuminated area on which the image analysis is performed was typically slightly smaller than the area of the probe A_0. For simplicity reasons we do however not distinguish these areas explicitly, but whenever necessary we corrected for the small difference.

The precise measurement of the growth dynamics of the cavities can unfortunately not be undertaken for the complete force-displacement curve. Due to loss of contrast and resolution we can only precisely track cavities until $\lambda = 3$–5, *i.e.* the first part the curves shown in fig. 4 and all the following results will be restricted to this elongation range.

The study of the evolution of the projected areas taken by the cavities A_b as a function of time and nominal elongation λ gives interesting insights on the growth dynamics of the cavities and can be linked to the rheological properties of the material and to the adhesion at the interface with the probe.

Cavity nucleation is, for the used materials, mainly determined by the presence of small defects at the interface between the sample and the probe. The spatial and time distribution of cavity nucleation are thus given by the spatial and size distribution of these defects and are

thus not reproducible between experiments [11]. The picture shown in fig. 1 thus has to be taken as an example of a typical distribution of cavity locations and sizes and it is not necessarily representative of all experiments. Interestingly, however, when the probe is pulled at $10\,\mu\mathrm{m\,s}^{-1}$ the function A_b/A_0 (shown in fig. 6a) is very reproducible for different experiments with the same material and is found to be similar for the three materials.

Contrary to the tests at $10\,\mu\mathrm{m\,s}^{-1}$, when the probe is pulled more slowly (at $1\,\mu\mathrm{m\,s}^{-1}$), see fig. 6b, some scatter is observed for A_b/A_0 for each material and A_b/A_0 now seems to depend on the material. Bg1110 shows a faster increase in the projected cavity area, then A1570 and A650. This indicates that at slow pulling rate a more interfacial growth is observed for the more elastic material, whereas the more viscous materials show a stronger growth in the bulk. This result is consistent with what was found by Yamaguchi *et al.* [4] for adhesives with different crosslink densities. The data can also be represented as the average cavity height $h_b/h_0 = A_0/A_b(\lambda - 1)$ (see fig. 6c and d) showing more clearly the differences observed for the different materials at slow pulling speed. Note that the data for λ close to 1 have not been represented as cavities are only detected when their size is larger than a given threshold. In particular in the beginning of the experiment the total surface covered by cavities A_b is thus underestimated leading to an overestimation of h_b/h_0. Furthermore in the beginning of the experiment some additional material from the adhesive film might be pulled under the probe leading to a small increase in total volume. Also this effect leads to an overestimation of h_b/h_0 and to the small decrease of the average cavity height with increasing λ observed in fig. 6.

The differences in the measurements between the two probe velocities are interesting. In fact, they show that at $10\,\mu\mathrm{m\,s}^{-1}$ the shape of the cavity is fully determined by the high frequency behavior of the materials, which does not vary much between the different materials. On the other hand, at $1\,\mu\mathrm{m\,s}^{-1}$, differences in rheological properties do lead to significantly different kinematics which will eventually lead to very different levels of dissipated energy.
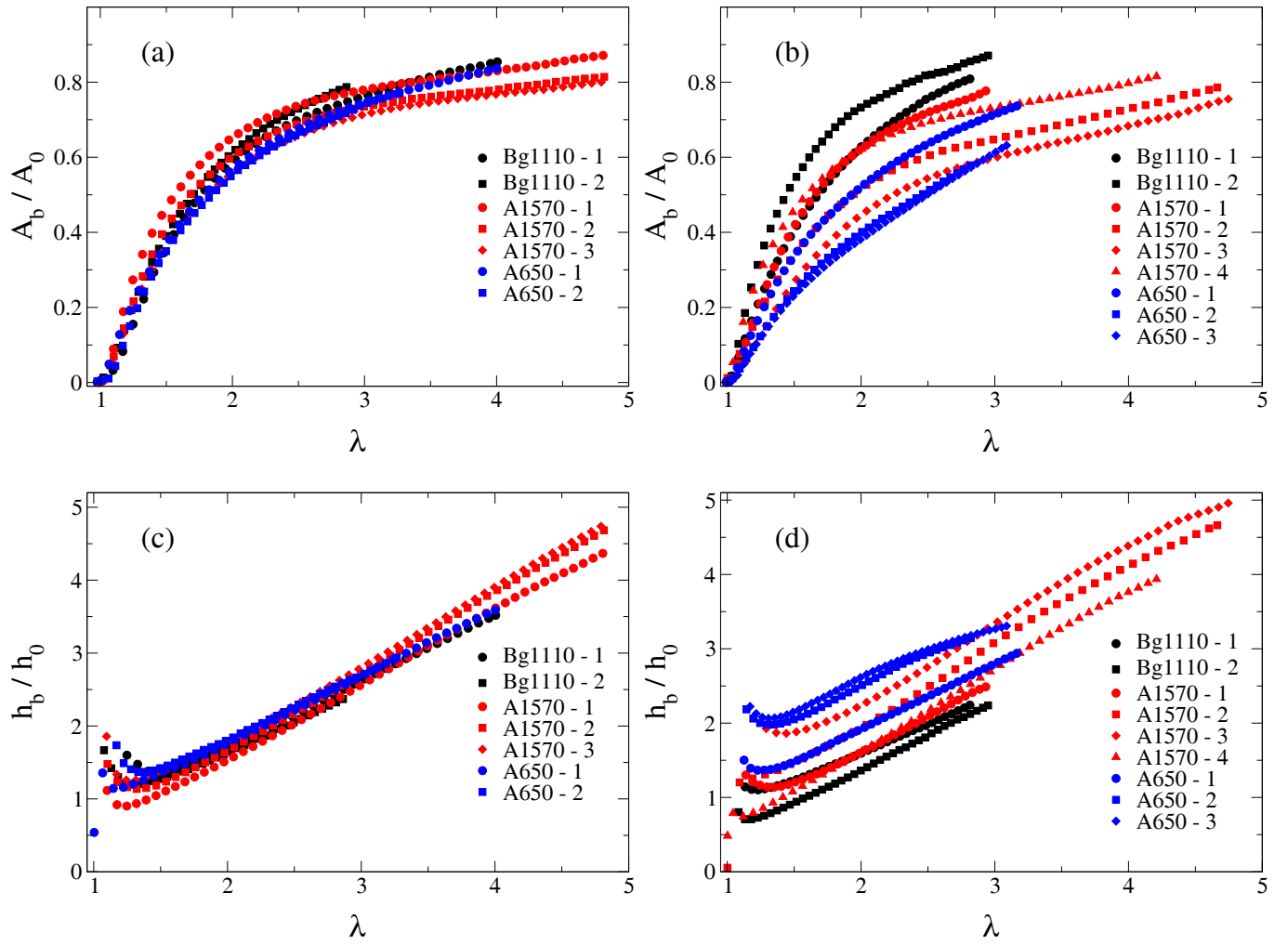
Fig. 6. Evolution of the normalized projected area covered by the cavities A_b/A_0 (a and b) and the normalized average cavity height h_b/h_0 (c and d) as function of the nominal elongation λ. These experiments were performed at a constant pulling velocity of $10\,\mu\mathrm{m\,s}^{-1}$ (a and c) and $1\,\mu\mathrm{m\,s}^{-1}$ (b and d).

3.4 Projected shape of cavities

During the early stages of the debonding process described in the previous paragraph, the shape of the projected area of individual cavities undergoes a transition from a circular to a more irregular form. Initially cavities grow in a circular manner. As the cavities start to occupy more volume they begin to feel each other through elastic interactions and viscoelastic flow. These interactions lead to a deviation from their initial circular shape and, eventually, to the coalescence of cavities, further modifying the overall shape. A simple way to quantify this geometrical transition is to compute the size of the difference between the shape of the cavity and the circle with the same projected area placed at the center of mass of the cavity, see fig. 7. This absolute difference between areas, A_d, provides a measure of the average change in shape of the cavities, thus quantifying in this way how the material responds to an external deformation. The elasticity of the material acts here like a surface tension and restricts sharp changes in shape [26].
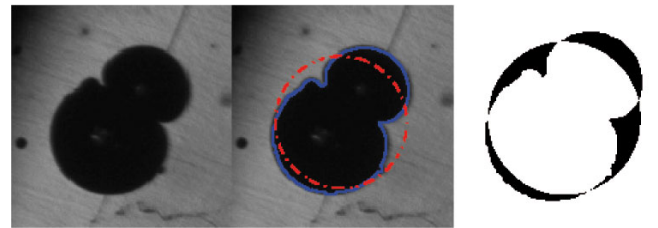

Fig. 7. Procedure to measure A_d. From left to right: i) Image of the cavity. ii) Detected perimeter (blue solid line) and equivalent circle (red dashed line) placed on the center of mass of the cavity. iii) Absolute difference between the two areas (black region).

The data is best shown as a function of the relative area occupied by cavities (A_b/A_0) as we expect their shape to evolve as a function of their interaction with each other. Note that similar trends are observed when plotting the results as a function of λ but, in particular at $1\,\mu\mathrm{m\,s}^{-1}$, the value of λ where $(A_b/A_0) = 0.5$ varies significantly
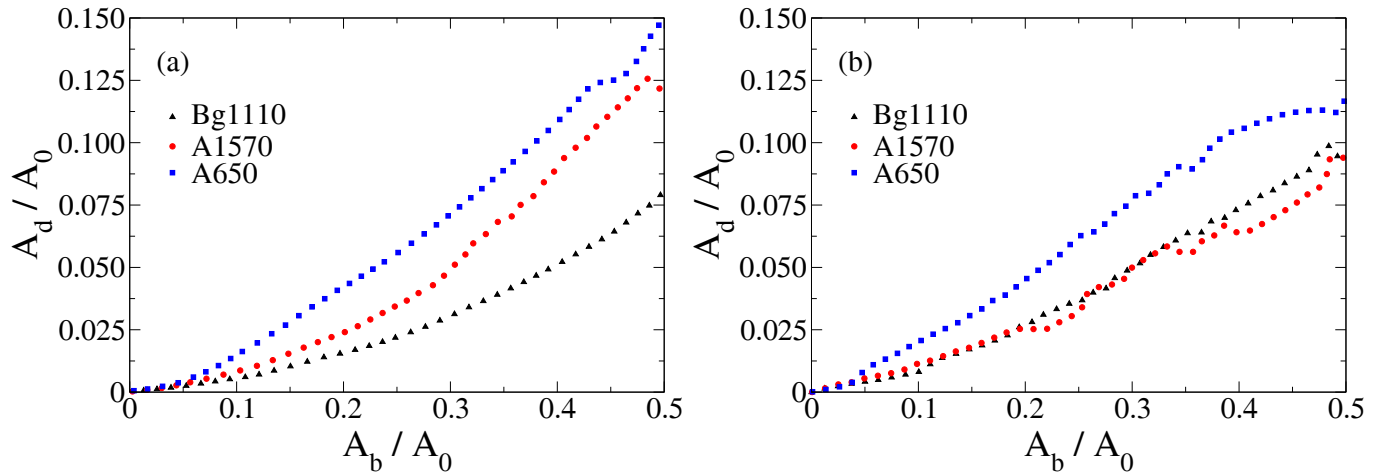
Fig. 8. Evolution of the equivalent cavity ellipticity A_d/A_0 as function of the load-bearing area A_b/A_0 at the pulling velocity of $10\,\mu\mathrm{m\,s^{-1}}$ (a) and $1\,\mu\mathrm{m\,s^{-1}}$ (b).

for different materials (see fig. 6) making the comparison difficult.

For all materials and strain rates, the projected area of the cavities becomes markedly non-spherical as cavities interact or merge with each other. The evolution of the normalized A_d/A_0 for the two velocities is shown in fig. 8. At both velocities the more elastic material Bg1110 maintains more circular cavities consistent with its more elastic character. This strongly suggests that the level of elastic energy stored in the material during deformation has an effect on the curvature of the cavities.

3.5 Growth rate of individual cavities

We estimate the growth rate of individual cavities from the evolution of the projected area of each cavity as a function of time shortly after their nucleation. Images of the whole probe have not enough resolution to provide this information and we thus use high magnification images ($5\times$) of the central part of the sample.

The increase in area of a single cavity normalized by the area of the probe is shown as a function of time in fig. 9. From this figure it is clear that the growth of cavities does not follow a simple functional form, in agreement with previous observations [11,16,18]. Right after nucleation, exponential cavity growth is observed [18], but quickly after this initial stage they start to interact with the surrounding cavities and their growth slows down and deviates from the exponential behavior. This is easily explained by the fact that cavities relax the accumulated stress in the adhesive layer very quickly after their nucleation, leading to a slow down of the growth.

We aim at capturing the first stages of cavity growth, as differences between different materials are expected to be important mainly when cavities grow independently. Even if cavities grow exponentially right after nucleation, the later stages of the growth rate can be approximated by a square root function and a simple exponential fit does not permit a clean estimation of the growth rate α. In fact,
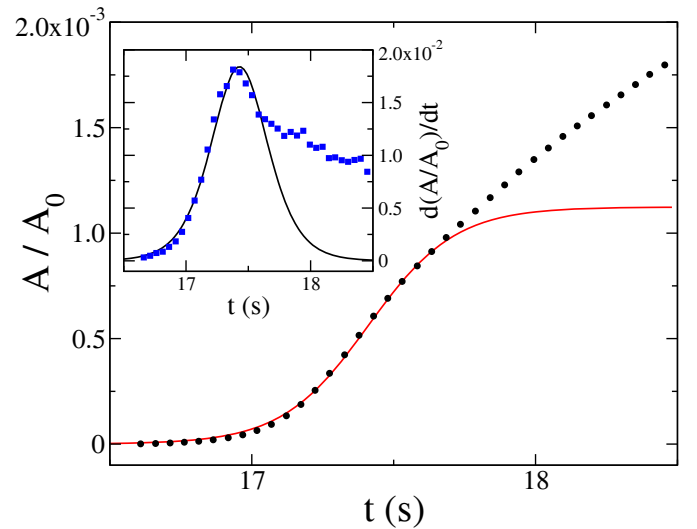

Fig. 9. Example of the evolution of the area of a growing cavity and its time derivative (inset) as a function of time and example of the fit procedure used to estimate α. Points are experimental data from digitalized images whereas solid lines correspond to fits of eqs. (3) and (4) (inset), respectively.

the time variation of the area $A(t)$ of each cavity reaches a maximum in a very short time and, subsequently, it decreases. From a practical point of view, it is easier to catch this change of behavior looking at the maximum of the growth velocity. In this way, all the data before and some data after this peak can be used for the estimation of the growth rate. This simple practical consideration allows one to increase the number of points used for the nonlinear fit (and hence its accuracy) compared to the estimation of the growth rate with a standard exponential function.

A sigmoid function S captures the initial exponential growth of $A(t)$ and its successive relaxation in a very compact functional form

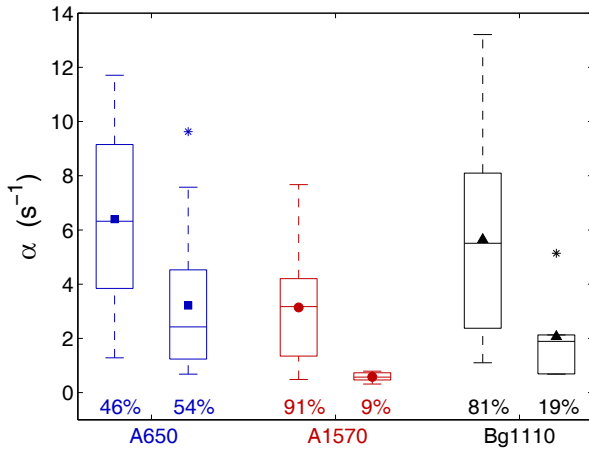$$S = a \left[1 + e^{-\alpha(t-t_0)}\right]^{-1}, \tag{3}$$

Fig. 10. Box plot of the growth rate α for the three different materials at the pulling velocity of $10\,\mu\mathrm{m\,s}^{-1}$. Cavities have been divided into two groups according to their nucleation time, before (left boxes) and after (right boxes) the force peak. Percentages show the proportion of cavities for each group. The total number of cavities were 39 for the A650, 53 for the A1570, and 32 for the Bg1110. The box plot is characterized by five-numbers summaries, *i.e.* the smallest observation (the lower horizontal line), the lower quartile (lower boundary of the box), the median (the line inside the box), the upper quartile (upper boundary of the box), and the largest observation (the upper horizontal line). We have also added the mean of each data set (the symbol inside the box) and outliers are represented by stars.

where a is the amplitude of S (for $a = 1$, $S \to 1$ when $t \to \infty$), α is the growth rate, and t_0 is the moment of maximum growth. These three parameters are estimated from a nonlinear least squares fit of the time derivative of A by using the function

$$\frac{\mathrm{d}S}{\mathrm{d}t} = \frac{a\alpha\,e^{-\alpha(t-t_0)}}{\left[1 + e^{-\alpha(t-t_0)}\right]^2}\,. \qquad (4)$$

A typical result of this fitting procedure is reported in fig. 9.

A box plot of the growth rate α for the three materials is shown in fig. 10. We have divided the cavities in two groups, those that have nucleated before the force peak during the probe-tack test (left column) and those nucleated after it (right column).

First of all, one can note that for the more elastic materials, Bg1110 and A1570, most of the cavities nucleate before the maximum of the stress peak is reached [17]. For the more liquid-like material however significant nucleation is observed even after the stress peak has been reached. This phenomenon can be explained by the fact that for the low modulus of the A650 material the compliance of the adhesive layer quickly drops below the compliance of the apparatus leading to a sudden transfer of energy from the apparatus to the adhesive layer initiating nucleation of further cavities. This observation is known

to be apparatus dependent [13,15,27]. The most interesting observation is the difference in growth rate between the different adhesives. The most elastic material, Bg1110, and the most liquid-like material, A650, both show larger growth rates with a large scatter, whereas the growth rate of the A1570 material is found to be smaller and more reproducible. For the Bg1110 the large growth rate of the projected area can be explained by the large amount of elastic energy stored in the elastic layer, leading to strong cavity growth along the interface (a crack propagation mechanism). For A650 the resistance of the material is too small to prevent bulk expansion of cavities, also leading to rapid growth of the projected area. The A1570 material seems to have the optimal material properties and leads to a moderate growth rate. The large scatter in the growth rate of cavities nucleated before the peak, observed for A650 and Bg1110, is most likely due to differential nucleation at different stress levels leading to different growth rates [11,16]. For A1570 the growth rate is dominated by the viscoelasticity of the material leading to smaller differences in the observed growth rates.

A detailed discussion of the criteria leading to different cavity shapes for different experimental conditions has also been carried out for simple silicone viscoelastic fluids by Teisseire *et al.* [28].

3.6 Effective normal stress

One of the most interesting results that comes from the detailed analysis of the kinematics of the debonding structure is the analysis of the applied force. The stress field in the material when many cavities are growing simultaneously is complex and cannot be measured directly as a function of position. However it is possible to use average quantities such as force and total projected area of the cavities A_b to infer average information.

The measured normal force F_T results from two contributions. The first one, F_m, arises from the elongation of the viscoelastic material, whereas the other contribution, F_P, is due to the work done against the atmospheric pressure to increase the volume of the low-pressure cavities (a suction cup effect) [13,14]. As our interest lies in the estimation of the viscous tensile stress inside the cavity walls, we first separate these two contributions. Then we use F_m to estimate the effective viscous stress applied to the load-bearing area, corresponding to the slice with the smallest cross-section.

In detail, the fraction of the measured force due to the work against the atmospheric pressure depends on the spatial distribution of the cavities on the sample. Yamaguchi *et al.* used a simple model to study the dynamics of debonding of an axisymmetric PSA simplified to a one-dimensional problem [19,20]. Their numerical investigations showed that, after nucleation of cavities, the pressure field rapidly drops to a value close to zero at the position of the two outermost cavities, leading to a screening effect on other cavities inside the PSA, in agreement with the findings of other authors [13,15]. A sketch of a typical pressure distribution can be seen in fig. 5. This result can
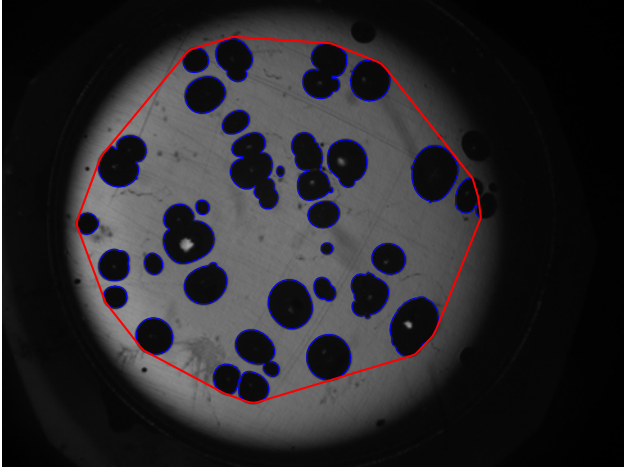
Fig. 11. Convex envelope of the region occupied by cavities (red solid line) with area A_c. Cavities with area smaller than the threshold $\epsilon_A = 50$ pixels are not taken into account. Also cavities nucleated at the border of the illuminated region are discarded because they lie outside the area our algorithm set as safe region for detection.

be easily extended to our two-dimensional arrangement of cavities by considering the convex envelope of the perimeters of the cavities. The dotted lines represent the position of the envelop of the cavities. As shown in fig. 11, this area A_c strongly depends on the location of cavities and can be obtained from the images, so that

$$F_P = A_c(P_{\mathrm{atm}} - P_b), \tag{5}$$

where P_b is the pressure inside the cavities and P_{atm} is the atmospheric pressure. As P_b is of the order of magnitude of the vapor pressure, $P_{\mathrm{atm}} \gg P_b$ and eq. (5) reduces to [14]

$$F_P \sim A_c P_{\mathrm{atm}}. \tag{6}$$

Although it is obvious that this crude calculation of the pressure field is not accurate in the nucleation region (before and around the force peak), it gives a good approximation after the force peak when many cavities are growing simultaneously in size.

We can then deduce $F_m = F_T - F_P$ and calculate the effective tensile component of the viscous stress in the slice where the cavities have their maximal diameter (*i.e.* where the projected area of the walls between cavities is minimum)

$$\sigma_e = \frac{F_m}{A_e}, \tag{7}$$

where $A_e = A_0 - A_b$.

3.7 Effective elongation

To plot an effective stress *versus* strain curve, we should not only consider an effective stress but also an effective elongation along the tensile direction for the position in the slice where the projected area of the walls between
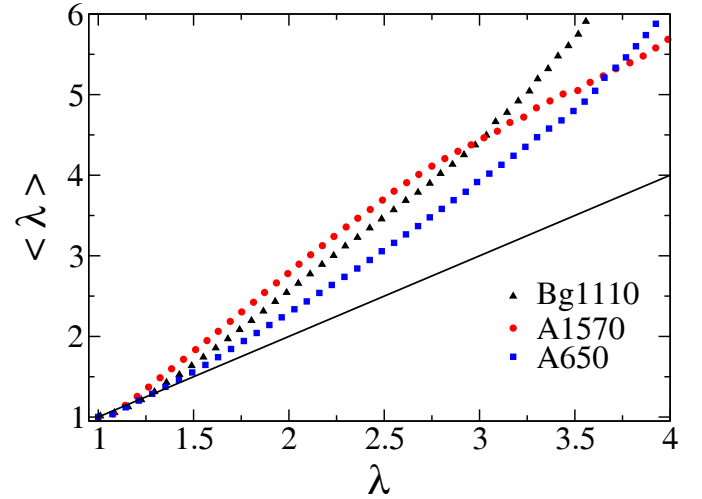

Fig. 12. Effective elongation $\langle \lambda \rangle$ *versus* nominal elongation λ for the three materials at a pulling velocity of $10\,\mu\mathrm{m\,s^{-1}}$. The black line is a guide for the eye with slope one.

cavities is minimum. Analogous to the correction of the nominal stress we now use the load-bearing area to write the effective elongation as

$$\langle \lambda \rangle = \frac{A_0}{A_e}. \tag{8}$$

The effective elongation differs from the nominal elongation $\lambda = h(t)/h_0$ due to the fact that the cavities do not necessarily occupy the whole height of the adhesive layer (see fig. 5). When considering the load-bearing area, corresponding to the slice with the minimal cross section, volume conservation does not apply. $\langle \lambda \rangle$ can thus be larger compared to λ.

In fig. 12 this effective average value of $\langle \lambda \rangle$ is plotted as a function of the nominal λ. The results show that the effective elongation always exceeds the nominal one, suggesting a localization of the deformation in the observation plane analogous to a necking process. The necking process appears to be unstable (*i.e.* the slope of $\langle \lambda \rangle$ *vs.* λ increases with increasing λ) for Bg1110 (crack propagation at the interface due to the stress concentration at the crack tip) and A650 (no strain hardening and cohesive failure) and stable for the A1570 which has the best PSA properties. This figure shows well how the elongational properties of the adhesives should be optimized. If too much elastic energy is stored during elongation, stresses at the edge of the cavities cannot relax and the cracks coalesce at a relatively low value of λ. If too little elastic energy is stored, the debonding geometry leads to necking and cohesive failure. This optimized set of properties is consistent with the PSA design rules proposed by Deplace *et al.* [6] and is also in agreement with the observations made on the growth rates from fig. 10.

3.8 Effective stress versus effective elongation curves

We can now discuss effective stress *versus* effective elongation curves as presented in fig. 13. The initial peak
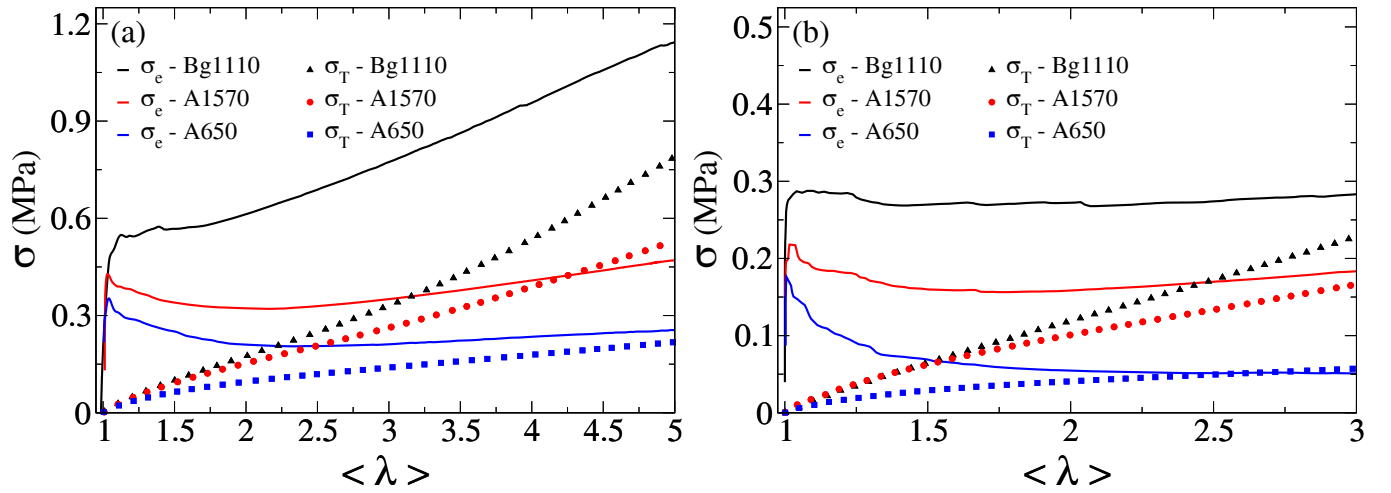
Fig. 13. Effective σ_e and true tensile σ_T stresses for the three materials at a pulling velocity of $10\,\mu\mathrm{m\,s^{-1}}$ (a) and $1\,\mu\mathrm{m\,s^{-1}}$ (b).

present in the nominal stress is not observed anymore for the Bg1110 material and is much less pronounced for the two other materials. At 1 and $10\,\mu\mathrm{m\,s^{-1}}$ the effective stress for the A650 keeps decreasing after the peak and leads, eventually, to cohesive failure. For the intermediate molecular weight (A1570) the effective stress decreases first and then slightly increases while the most interesting behavior occurs for the Bg1110 where the effective stress never decreases after the peak force. One would expect the true stress to be much more directly related to the material properties and it is clear by qualitatively comparing fig. 13 for example with fig. 3, that the elasticity influences greatly how the effective stress varies with extension. The increase in effective stress for the Bg1110 is clearly related to the cavities expanding laterally as cracks and this increase in effective stress reflects the presence of a stress concentration at the cavity edge which leads to eventual coalescence of adjacent cavities and debonding. The moderate increase in true stress of the other two materials is characteristic of the extension of the walls between cavities.

To go even further, we can finally compare the effective stress σ_e as function of $\langle\lambda\rangle$ with the true stress $\sigma_T = F/A(t)$ (which, due to incompressibility, can be calculated by $\sigma_T = \lambda\sigma_N$) obtained from the tensile test (fig. 3). Our correction of the stress and strain values from the debonding experiments using the load-bearing area is a first attempt to obtain effective stress strain curves that can reasonably be compared to results from material characterization obtained by traction experiments. The results of this comparison are shown in fig. 13a and b. Obviously the two stresses are very different at values of λ close to 1, since the degree of confinement is very high [7,29]. However, as the elongation of the adhesive layer increases the effective stress should become closer to the tensile stress in uniaxial extension since the walls between cavities are not confined anymore. This is qualitatively observed in fig. 13a and b but one should keep in mind that the stress remains highly heterogeneous in the foam structure and is far from being uniaxial. Note also that for the slow pulling speed

the contribution of F_P is more important compared to the faster pulling velocity and small errors made by our approximations might thus be more important for this case. The most striking difference is between the A1570 and Bg1110 where an apparently small difference in uniaxial constitutive behavior (dotted lines in fig. 13a and b) leads to a much larger difference in effective stress when plotted as a function of effective elongation and finally to completely different debonding mechanisms (see fig. 4).

4 Conclusions

We have carried out a systematic investigation of the kinematics of deformation of thin model adhesive layers made from acrylic pressure-sensitive adhesives, as they are debonded from a flat-ended cylindrical probe at two different probe velocities.

The rheological properties of the three adhesives were characterized in the linear viscoelastic regime and in uniaxial extension until rupture at two different strain rates. The three adhesives were chosen to show differences in mechanical behavior at low frequency in small strain and at large strain due to variable levels of molecular weight and chain branching.

The debonding of the layer from the probe occurred through the nucleation and growth of cavities which then led to an elongated foam structure. However, the relationship between the applied force and the nominal elongation were markedly different for the three adhesives representative of behaviors spanning from too liquid-like to too solid-like.

The kinematics of the deformation of the layer was characterized by image analysis as a function of time and the three materials were systematically compared. The average shape of the cavities nucleating during debonding and the total projected area of the cavities in the plane of the adhesive film were characterized quantitatively for all three materials at two different velocities.

Very few differences in the overall projected area were observed at $V = 10\,\mu\mathrm{m\,s}^{-1}$. However, cavities showed more spherical projected areas for the more elastic adhesive at $1\,\mu\mathrm{m\,s}^{-1}$ while cavities were the most irregularly shaped for the lower molecular weight adhesive. Furthermore an estimate of the effective tensile strain in the plane of observation showed that the effective tensile strain systematically exceeds the nominal strain and diverges for the lowest molecular weight (leading to cohesive debonding) and the most elastic adhesive (leading to interfacial failure by crack propagation) and was only stable for the intermediate adhesive showing the best PSA properties.

The kinematic information was used to calculate for the first time to our knowledge the effective stress as a function of time in the stage where cavities grow mostly in the plane of the film and are not yet very elongated in the tensile direction. While this effective stress drops after the peak force for the two uncrosslinked materials, it keeps increasing after the peak force for the Bg1110. Such a qualitative difference leads to an entirely different debonding mechanism, with stable fibrils for the two uncrosslinked materials and crack coalescence for the more elastic Bg1110.

These results show that small differences in rheological properties in small and in particular large strain, lead to significant changes in the kinematics of deformation under the same applied boundary conditions, which then has a great influence on the work of debonding. This coupling between rheological properties and kinematics is a great challenge for modeling soft materials and we hope that our results will be the base of comparison with simulations of computational fluid mechanics using realistic material properties.

Appendix A. Image processing

We developed an image analysis tool based on simple thresholding conversion. The algorithm starts with a calibration routine before the nucleation of cavities. In this first step, through a trial and error procedure, we estimate the critical level τ_0 (with $0 < \tau_0 < 1$) for the conversion from greyscale to binary image. Besides, we determine the region of the image within which we run our detection routine for the cavities. This region is established at the beginning of the image recognition procedure and does not evolve with time. The algorithm assigns to each cavity an index and manages dynamically the events of nucleation and coalescence (for details see point 4). Obviously, an empty list is created at the start of the procedure. Then, the algorithm repeats the following steps for each frame:

1. The image is filtered with a low pass filter in order to reduce its noise content, we typically use a simple averaging over windows of size 3×3 pixels.

2. The format of the image is converted from greyscale to binary according to τ_0, that is, all the pixels with luminance smaller than τ_0 are mapped to 1 (white) while the others to 0 (black).

3. All the connected regions with area smaller than a threshold ϵ_A are removed. This step is easily implemented by morphologically opening the binary image.

4. The boundaries between black and white regions are traced and labeled with an index. The children of each parent object are discarded in order to avoid the wrong detection of small cavities inside a large encompassing cavity. These white spots are created by the unscattered light that passes through the cavity and is reflected back from the steel substrate. Although their position and their extension is related to the contact region of the cavity with the steel substrate, these quantities are very sensitive to many irreproducible factors, such as the intensity of the light, the magnification factor and the sample alignment. For this reason these white spots are not taken into account in the analysis of the images from whole probe experiments.

5. For each cavity several geometrical quantities are measured, *e.g.* its center of mass, area, equivalent diameter, and eccentricity.

6. By comparing the center of mass of cavities in the current and the previous frame, the index of each cavity is changed according to the list of indexes of the previous frame. In this step the processes of nucleation and coalescence of cavities are handled. For each new nucleated cavity a new entry in the list is created with a new index $n_T + 1$, where n_T is the largest index of the list. However, when the coalescence of two or more cavities occurs, the new data of the coalesced cavity are assigned to the lowest index in the list while the entries of the other cavities are deleted. In this manner we are able to track the evolution of each cavity and record all the coalescence events.

References

1. J. Nase, C. Creton, O. Ramos, L. Sonnenberg, T. Yamaguchi, A. Lindner, Soft Matter **6**, 2685 (2010).
2. Y. Urahama, J. Adhes. **31**, 47 (1989).
3. H. Lakrout, P. Sergot, C. Creton, J. Adhes. **69**, 307 (1999).
4. T. Yamaguchi, K. Koike, M. Doi, EPL **77**, 64002 (2007).
5. A. Zosel, Int. J. Adhes. Adhes. **18**, 265 (1998).
6. F. Deplace, C. Carelli, S. Mariot, H. Retsos, A. Chateauminois, K. Ouzineb, C. Creton, J. Adhes. **85**, 18 (2009).
7. A.J. Crosby, K.R. Shull, H. Lakrout, C. Creton, J. Appl. Phys. **88**, 2956 (2000).
8. J. Nase, A. Lindner, C. Creton, Phys. Rev. Lett. **101**, 074503 (2008).

9. K.R. Shull, C.M. Flanigan, A.J. Crosby, Phys. Rev. Lett. **84**, 3057 (2000).
10. J. Nase, D. Derks, A. Lindner, Phys. Fluids **23**, 123101 (2011).
11. A. Chiche, J. Dollhofer, C. Creton, Eur. Phys. J. E **17**, 389 (2005).
12. I. Chikina, C. Gay, Phys. Rev. Lett. **85**, 4546 (2000).
13. S. Poivet, F. Nallet, C. Gay, P. Fabre, Europhys. Lett. **62**, 244 (2003).
14. S. Poivet, F. Nallet, C. Gay, J. Teisseire, P. Fabre, Eur. Phys. J. E **15**, 97 (2004).
15. M. Tirumkudulu, W.B. Russell, T.J. Huang, Phys. Fluids **15**, 1588 (2003).
16. Y. Peykova, S. Guriyanova, O.V. Lebedeva, A. Diethert, P. Müller-Buschbaum, N. Willenbacher, Int. J. Adhes. Adhes. **30**, 245 (2010).
17. Y. Peykova, O.V. Lebedeva, A. Diethert, P. Müller-Buschbaum, N. Willenbacher, Int. J. Adhes. Adhes. **34**, 107 (2012).
18. K. Brown, J.C. Hooker, C. Creton, Macromol. Mater. Eng. **287**, 163 (2002).
19. T. Yamaguchi, H. Morita, M. Doi, Eur. Phys. J. E **20**, 7 (2006).
20. T. Yamaguchi, H. Morita, M. Doi, Eur. Phys. J. E **21**, 331 (2006).
21. G. Josse, P. Sergot, C. Creton, M. Dorget, J. Adhes. **80**, 87 (2004).
22. A. Lindner, T. Maevis, R. Brummer, B. Lühmann, C. Creton, Langmuir **20**, 9156 (2004).
23. L.V. Mohite, D. Auhl, M. Ahmadi, F. Tanguy, C. Creton, J.T Padding, C. Bailly, submitted (2013).
24. C. Creton, H. Lakrout, J. Polym. Sci. Pol. Phys. **38**, 965 (2000).
25. A. Zosel, Colloid Polym. Sci. **263**, 541 (1985).
26. J. Dollhofer, A. Chiche, V. Muralidharan, C. Creton, C.-Y. Hui, Int. J. Solids Struct. **41**, 6111 (2004).
27. B.A. Francis, R.G. Horn, J. Appl. Phys. **89**, 4167 (2001).
28. J. Teisseire, F. Nallet, P. Fabre, C. Gay, J. Adhes. **83**, 613 (2007).
29. K.R. Shull, C. Creton, J. Polym. Sci. Pol. Phys. **42**, 4023 (2004).